Journal of Advanced Ceramics
2024, **13**(11): 1737–1747
https://doi.org/10.26599/JAC.2024.9220970

Research Article

Balancing the piezoelectric coefficient and carrier concentration of Bi_2WO_{6-x} for ultrahigh piezocatalysis

Ying Wang[1], Xiaoli Xu[1,2,✉], Lingbo Xiao[3], Lutao Li[4,5], Qiuhua Xu[2,6], Zhenhai Wen[2,6], Laishun Qin[1,✉], Yanmin Jia[7], Dong-Liang Peng[8], Wanping Chen[9], Da Chen[1,✉]

[1] *College of Materials and Chemistry, China Jiliang University, Hangzhou 310018, China*
[2] *Key Laboratory of Jiangxi Province for Persistent Pollutants Control, National-Local Joint Engineering Research Center of Heavy Metals Pollutants Control and Resource Utilization and Resources Recycle, Nanchang Hangkong University, Nanchang 330063, China*
[3] *Department of Physics, Zhejiang University of Science and Technology, Hangzhou 310008, China*
[4] *Jiangsu Key Laboratory for Science and Applications of Molecular Ferroelectrics, Southeast University, Nanjing 211189, China*
[5] *Key Laboratory of Advanced Carbon Materials and Wearable Energy Technologies of Jiangsu Province, College of Energy, Soochow University, Suzhou 215006, China*
[6] *State Key Laboratory of Structural Chemistry, and Fujian Provincial Key Laboratory of Materials and Techniques toward Hydrogen Energy, Fujian Institute of Research on the Structure of Matter, Chinese Academy of Sciences, Fuzhou 350002, China*
[7] *School of Physics and Information Technology, Shaanxi Normal University, Xi'an 710121, China*
[8] *State Key Laboratory of Physical Chemistry of Solid Surface, Fujian Key Laboratory of Surface and Interface Engineering for High Performance Materials, College of Materials, Xiamen University, Xiamen 361005, China*
[9] *School of Physics and Technology, Wuhan University, Wuhan 430072, China*

Received: June 15, 2024; Revised: August 22, 2024; Accepted: September 15, 2024

Abstract: Balancing the piezoelectric coefficient and carrier concentration of materials is key in the field of piezocatalysis. In this work, Bi_2WO_6 material with both piezoelectric and semiconductor properties was chosen as a model material. A one-step ethylene glycol (EG)-assisted solvothermal method was used to synthesize Bi_2WO_6 with oxygen vacancies. By controlling the solvothermal time and temperature, the oxygen vacancy concentration (C_{OV}) was regulated. As C_{OV} increases, the piezoelectric coefficient decreases, the carrier concentration increases, and the hydrogen production rate first increases but then decreases. When C_{OV} reaches 1.45×10^{12} spins·mg^{-1}, the corresponding piezoelectric coefficient and carrier concentration are 13.9 pm·V^{-1} and 2.90×10^{20} cm^{-3}, respectively. The optimal hydrogen production rate per power of 2.21 μmol·g^{-1}·h^{-1}·W^{-1} is equivalent to or even better than that of most reported piezocatalysts. The piezoelectric coefficient and carrier concentration, as two factors, jointly determine the piezocatalytic performance. The findings of this research can provide important and deep-seated insights for better piezocatalysts in the future.

Keywords: piezocatalysis; oxygen vacancy; carrier concentration; piezoelectric coefficient; hydrogen evolution

1 Introduction

As a renewable energy source, hydrogen has a series of advantages, such as being green and low-carbon, highly efficient, and convenient to store, and it is gradually becoming an important carrier for the development of global energy transformation [1–5]. Vibration energy, such as water flow, tides, and human activities, is a common form of clean energy in nature [6–9]. The use of mechanical energy is not limited by geography or time. Therefore, using piezoelectric materials to collect vibration energy for electrochemical redox reactions and realizing piezocatalytic water splitting is a promising method for hydrogen production [6,10,11]. The principle of piezocatalytic hydrogen evolution is that when external vibration acts on a piezoelectric material, positive (q^+) and negative (q^-) charges are generated on its surface, and q^- reacts with H^+ in water to form H_2 [12]. From the perspective of economic development, energy shortages, and environmental protection, the production of hydrogen by piezocatalysis without light or electricity dependence is of strategic importance and practical value [13].

The piezocatalytic effect is the product coupling of the piezoelectric effect and the electrochemical redox effect of materials [14,15]. Therefore, the piezocatalytic efficiency depends on the piezoelectric properties of the material, the carrier concentration (N_d) and mobility, the number of active sites, etc. The piezoelectric potential is a prerequisite for the piezocatalytic reaction [16]. For the water splitting reaction, the piezoelectric potential generated by the piezoelectric material must be greater than the Gibbs free energy change of 1.23 V [17]. The piezoelectric potential (V_{piezo}) can be described by Eq. (1) [18]:

$$V_{piezo} = \frac{d_{piezo} \cdot \sigma \cdot \omega}{\varepsilon} \quad (1)$$

where d_{piezo} is the piezoelectric coefficient of the material, σ is the applied stress, ω is the thickness of the material, and ε is the

✉ Corresponding authors.
E-mail: X. Xu, xiaolixu@cjlu.edu.cn;
L. Qin, qinlaishun@cjlu.edu.cn;
D. Chen, chenda@cjlu.edu.cn

dielectric constant of the material. It can be inferred that the greater the piezoelectric coefficient of the material is, the greater the output piezoelectric potential under vibration, which is conducive to improving the piezocatalytic efficiency.

Yuan *et al.* [19] used a Sm-doped $Pb(Mg_{1/3}Nb_{2/3})O_{3-x}PbTiO_3$ piezoelectric solid solution (with a piezoelectric coefficient (d_{33}) of ~1500 pC·N^{-1}) to study piezocatalysis and reported that its piezocatalytic activity changed almost linearly with d_{33}. Sun *et al.* [20] built a room-temperature multiphase coexistence system by reducing the phase transition temperature of lead-free $K_{0.5}Na_{0.5}NbO_3$-based piezoelectric materials, which improved their piezoelectric performance and finally increased the piezocatalytic reaction rate by 2.12 times. High piezoelectric performance can enhance the built-in electric field of a material, which is conducive to carrier separation and transport, and realize improved piezocatalytic performance. However, current research focuses on how to improve the piezoelectric properties of materials to obtain higher piezocatalytic activity. Although traditional ferroelectric materials have relatively high d_{33}, their intrinsic N_d is relatively low, which is not conducive to the generation of free charge in the piezoelectric process, thus affecting their piezocatalytic activity [21–23]. Defect engineering can adjust the electrical properties of materials by introducing atomic defects, which is an effective method to significantly improve N_d of materials [24–27]. Among them, the positive role of oxygen vacancy regulation in defect engineering has been proven in the field of catalysis, which can 1) facilitate carrier separation. Oxygen vacancies promote exciton-to-carrier conversion, accelerate surface reduction half-reactions, and promote carrier separation. For example, Zhang's team [28] prepared $Sr_2Bi_2Nb_2TiO_{12}$ nanosheets with oxygen-rich vacancies for photocatalytic CO_2 reduction. The CO formation rate reached 17.11 μmol·g^{-1}·h^{-1}, and the reaction performance improved nearly 58-fold with the introduction of oxygen vacancies. In addition, the introduction of oxygen vacancies can also 2) increase the number of reaction active sites. Wu's team [29] introduced oxygen vacancies on $ZnSnO_3$ nanowires to increase the number of reactive sites, improving the piezocatalytic hydrogen production rate to 3453.1 μmol·g^{-1}·h^{-1}. However, the introduction of oxygen vacancies may affect the ordered arrangement of electric dipoles in ferroelectric materials, thus destroying their piezoelectric properties to a certain extent. Therefore, balancing d_{33} and N_d values of materials is a key scientific problem in the field of piezocatalysis.

Bismuth tungstate (Bi_2WO_6) is the simplest oxide in the bismuth layer perovskite family, with an energy band gap (E_g) of approximately 2.75 eV; it is a semiconductor material with an indirect bandgap transition, and its special layered perovskite structure is conducive to carrier transport [30,31]. Moreover, Bi_2WO_6 has good piezoelectric properties. d_{33} of Bi_2WO_6 ceramics is 15 pC·N^{-1}, and d_{33} of Bi_2WO_6 single crystal is 40 pC·N^{-1}, which has obvious advantages over other piezoelectric semiconductors such as ZnO (d_{33} = 22.5 pm·V^{-1}) and is comparable to that of ferroelectric barium titanate (d_{33} of barium titanate nanowire is 45 pC·N^{-1}) [32]. In addition, the conduction band (CB) position of Bi_2WO_6 is more negative than the hydrogen reduction potential [32], indicating the feasibility of water splitting for hydrogen production. To study the relationship between d_{33} and N_d on the piezocatalytic performance, Bi_2WO_6, which has both piezoelectric [32] and semiconductor properties [33], was chosen as a model material.

In this work, a simple one-step ethylene glycol (EG)-assisted solvothermal method was used to prepare Bi_2WO_{6-x} nanoparticles with original oxygen vacancies. By controlling the solvothermal time and temperature, the oxygen vacancy concentration (C_{OV}) was regulated. The correlation and influence between oxygen vacancies and the piezocatalytic performance of hydrogen generation were comprehensively analyzed from the aspects of d_{33}, N_d, carrier separation and migration mechanisms, and surface catalytic activity. The optimal hydrogen production rate per power of 2.21 μmol·g^{-1}·h^{-1}·W^{-1} is equivalent to or even better than that of most reported piezocatalysts. d_{33} and N_d, as two factors, jointly determine the piezocatalytic performance. The findings of this research can provide important and deep-seated insights for better piezocatalysts in the future.

2 Experimental

2.1 Chemical reagents

All materials and solvents were of analytical grade and used without any further purification. Sodium tungstate dihydrate ($Na_2WO_4·2H_2O$; ≥ 99.5%), ethanol, C_2H_5OH (≥ 99.7%), and ethylene glycol ($C_2H_6O_2$ (EG); ≥ 98.0%) were supplied by Shanghai Macklin Biochemical Co., Ltd., China. Bismuth(III) nitrate pentahydrate ($Bi(NO_3)_3·2H_2O$; ≥ 99.0%) was purchased from Sinopharm Chemical Reagent Co., Ltd., China. Anhydrous sodium sulfate (Na_2SO_4; ≥ 99.0%) was acquired from Hangzhou Gaojing Fine Chemical Industry Co., Ltd., China. Deionized water was procured from Meek Chemical Co., Ltd., China, and methanol (MeOH; ≥ 99.5%) was obtained from Aladdin, China.

2.2 Catalyst fabrication

Common methods of introducing oxygen vacancies include solvothermal reduction methods, high-temperature hydrogen reduction, atomic doping, plasma etching, etc. [34]. Considering cost, operation, and safety issues, solvothermal reduction methods have been extensively investigated [35]. In this work, ethylene glycol (EG) was used as a reducing agent to synthesize the original Bi_2WO_{6-x} with oxygen vacancies. By controlling the solvothermal time and temperature, the concentration of oxygen vacancies can be easily regulated. The fabrication procedures are shown in Fig. S1 in the Electronic Supplementary Material (ESM). In summary, 1.6 mmol of $Na_2WO_4·2H_2O$ was dissolved in 24 mL of EG and stirred until clear, which was denoted as solution A. Then, 56 mL of EG solution containing 3.2 mmol of $Bi(NO_3)_3·5H_2O$ was similarly stirred to a clear state and denoted as the solution B. The solution A was slowly dropped into solution B, stirred for 1 h at room temperature, and transferred to 100 mL teflon-lined stainless steel autoclaves. By controlling the solvothermal time and temperature, the C_{OV} was regulated, which was maintained at 180 °C for 12 h, 160 °C for 20 h, and 180 °C for 20 h (denoted Bi_2WO_{6-x}-1, Bi_2WO_{6-x}-2, and Bi_2WO_{6-x}-3, respectively). The obtained products were collected by centrifugation, washed three times with deionized water and ethanol, and dried in a vacuum oven (D2F-6050 ABF, Shanghai Kuntian Experimental Instrument Co., Ltd., China) at 60 °C for 12 h. The oxygen vacancy-free sample Bi_2WO_6 was obtained through annealing treatment at 400 °C for 4 h in an air-rich atmosphere.

2.3 Material characterizations

An X-ray diffractometer (XRD; Smart Lab-SE, Rigaku, Japan) collected data with Cu Kα (λ = 0.15406 nm) radiation at a scanning rate of 10 (°)·min^{-1}. A high-resolution transmission electron microscope (HRTEM; JEM-2100Plus, JEOL, Japan) obtained images. The surface morphology and corresponding mapping of the as-synthesized samples were investigated by a

scanning electron microscope (SEM; German Sigma 300, ZEISS, Germany). Energy dispersive X-ray spectroscopy (EDS) element mapping was used to analyze the types and contents of the microcomponent elements in the material. Adsorption–desorption isotherms were measured on a gas adsorption analyzer (ASAP 2460, Micromeritics, USA) at 77.30 K. Photoluminescence (PL) spectra were obtained from a photoluminescence spectroscope (F97Pro19057, Shanghai Lengguang Technology Co., Ltd., China) with a gas lamp as the excitation source and an excitation wavelength of 292 nm. The chemical composition, state, stress, vibration, and other information of the materials were obtained via a Raman spectrometer (Jobin Yvon, Horiba, France) with a He–Ne laser with a wavelength of 663 nm. An X-ray photoelectron spectroscope (XPS; K-Alpha, Thermo Scientific, USA) was used to record spectra under Al Kα ($h\nu$ = 1486.6 eV) irradiation. All binding energies were determined via the use of the C peak (284.8 eV) as a reference for calibration. An electron paramagnetic resonance (EPR) spectroscope (EMXplus-6/1, Bruker, Germany) was conducted to monitor the oxygen vacancy signals of the samples. Piezoresponse force microscopy (PFM) amplitude butterfly loops and Kelvin probe force microscopy (KPFM) were carried out via an atomic force microscope (Dimension Icon, Germany). Ultraviolet–visible (UV–Vis) diffuse reflectance spectrometer (UV-3600i Plus, SHIMADZU, Japan) performed within the range of 200–800 nm. The bandgap widths were calculated from Tauc plots; that is, $(ahv)^2$–(hv) plot can obtain a linear absorption edge, and the intercept of the linear absorption edge extending in the reverse direction on the X axis is the band gap.

2.4 Electrochemical measurements

The specific experimental process was as follows: 10 mg of piezocatalyst was uniformly mixed first with 10 μL of ethanol and then with 10 μL of nafion. The paste was then uniformly coated onto one side of an indium tin oxide (ITO) glass. The area of the electrode coated with the catalysts was 1 cm^2. Mott–Schottky plots were measured at a frequency of 1 kHz in a conventional three-electrode cell on an electrochemical workstation (CHI660E, China) with piezocatalysts loaded on ITO glass as the working electrode, a saturated calomel electrode (SCE) as the reference electrode, a platinum plate as the counter electrode, and a Na_2SO_4 solution (0.5 M) as the electrolyte. The electrochemical impedance spectra (EIS) Nyquist curves under no vibration and piezocurrent under vibration at a frequency of 40 kHz were measured with Ag/AgCl as a reference electrode. A double-sided conductive copper adhesive was used between the ITO glass and the samples to strengthen the adhesion.

2.5 Evaluation of piezocatalytic water splitting

The piezocatalytic performance of the catalysts was evaluated by hydrogen production from water splitting with an ultrasonic machine (KQ-100VDV, 60–100 W, and 45 kHz). The specific experimental process was as follows: 20 mg of piezocatalyst was added to 13.5 mL of deionized water and 1.5 mL of MeOH in glass bottles. The glass bottles were ventilated with Ar gas for 10 min to eliminate the effect of air and then sealed. The sealed bottle was subsequently placed in an ultrasonic machine, and the system temperature was maintained at 30–35 °C in the dark. Hydrogen production was measured through off-line sampling with a needle tube on a gas phase chromatography (GC-7820, Beijing Zhongke Huifen Instrument Co., Ltd., China). The comparative experiment of piezoelectric hydrogen production for each group of samples was repeated at least three times to avoid human error as much as possible.

3 Results and discussion

3.1 Material characterization

To synthesize Bi_2WO_{6-x} with different C_{OV}, the solvent-thermal synthesis and high-temperature annealing methods were adopted (see the Experimental Section, written as Bi_2WO_6, Bi_2WO_{6-x}-1, Bi_2WO_{6-x}-2, and Bi_2WO_{6-x}-3, respectively). The noncentrosymmetric crystal structures of Bi_2WO_6 and Bi_2WO_{6-x}-2 are presented in Figs. S2(a) and S2(b) in the ESM. Figure 1(a) shows the XRD patterns of Bi_2WO_{6-x} from 2θ values of 20° to 90° with different C_{OV}. All the diffraction peaks agree with the characteristic peaks of orthorhombic-phase Bi_2WO_6 (PDF#79-2381, *Pca*21 space group, *mm*2 point group) and indicate high crystallinity and purity [32]. Compared with those of Bi_2WO_{6-x}, the main diffraction peaks of Bi_2WO_6 samples are dramatically greater in intensity. XRD patterns of Bi_2WO_{6-x}-2 and Bi_2WO_{6-x}-2 after being annealed in Ar and air atmospheres (Fig. S3 in the ESM) clearly show that the XRD peak intensity of Bi_2WO_{6-x}-2 after annealing in Ar gas is stronger than that of Bi_2WO_{6-x}-2 but relatively weaker than that after annealing in air. After annealing in Ar, oxygen vacancies were introduced into the Bi_2WO_{6-x}-2 samples [36]. Both the annealing treatment and the introduction of oxygen vacancies affect the crystallization properties of materials [34,37]. However, annealing is the primary factor for enhanced crystallinity in this work. In addition, the XRD diffraction peak width narrows sequentially from Bi_2WO_{6-x} to Bi_2WO_6 owing to the larger grain size of Bi_2WO_6 after high-temperature annealing through an Ostwald ripening process [38]. The adjacent partially enlarged XRD patterns (Fig. 1(b)) clearly show that the 2θ value corresponding to (131) has the following relationship: Bi_2WO_{6-x}-3 < Bi_2WO_{6-x}-2 < Bi_2WO_{6-x}-1 < Bi_2WO_6. Owing to the presence of oxygen vacancies, the lattice spacing becomes larger, resulting in a smaller 2θ value [39]. Therefore, it can be preliminarily concluded that the C_{OV} of the four samples are in the order of Bi_2WO_6 < Bi_2WO_{6-x}-1 < Bi_2WO_{6-x}-2 < Bi_2WO_{6-x}-3. The microstructure details of the samples can be obtained from the HRTEM images (Figs. 1(c) and 1(d)). The marked fringes with d spacings of 0.31 and 0.33 nm can be indexed to the (131) crystallographic planes of orthorhombic-phase Bi_2WO_6 and Bi_2WO_{6-x}, respectively. The larger lattice spacing of Bi_2WO_{6-x}-2 than Bi_2WO_6 corresponds well with the XRD results. In addition, clear lattice fringes are observed at the edges of Bi_2WO_6; however, Bi_2WO_{6-x}-2 has a disordered layer of approximately 3.0–4.0 nm thickness at the sample edges (Fig. 1(d)). This phenomenon can be attributed to surface damage owing to the loss of oxygen and the formation of oxygen vacancies during the glycol-assisted solvothermal reaction process [37,40,41].

SEM images reveal the small grain sizes of the samples; however, accurate values cannot be obtained directly (Figs. S4(a) and S4(b) in the ESM). Therefore, HRTEM was adopted to visualize the samples more clearly (Figs. S5(a) and S5(c) in the ESM). The corresponding diameter distributions are shown in Figs. S5(b) and S5(d) in the ESM. Error analysis was performed to determine the average particle size of Bi_2WO_{6-x}-2 (10.26±0.25 nm), which was smaller than that of Bi_2WO_6 (23.41±0.38 nm). The smaller the particle size is, the larger the specific surface area of the sample [42]. Here, the specific surface areas of Bi_2WO_6 and Bi_2WO_{6-x}-2 are 23.68 and 88.90 $m^2 \cdot g^{-1}$, respectively (Fig. 1(e)). In catalysis, the size of the specific surface area is critical to the

number of reactive sites, as well as to the contact area between the catalyst and the reactants. In general, a material with a larger surface area has a relatively larger number of active sites and a larger contact area with the reactants, in turn leading to better catalytic activity [43,44]. Jia *et al.* [45] reported that the amorphous structure of a catalyst surface contains a significant number of unsaturated atomic dots or dangling bonds, thereby providing numerous active sites and increasing the catalytic activity. In addition, the elemental composition of Bi_2WO_6 with and without oxygen vacancies was investigated via EDS element mapping analysis, in which Bi, W, and O were uniformly distributed on the surfaces of Bi_2WO_6 and Bi_2WO_{6-x}-2 (Figs. S6(a)–S6(h) in the ESM). The mappings reveal homogeneous distributions of all the elements, further indicating that the oxygen vacancy-introducing process does not induce other factors, such as chemical inhomogeneity [25,46].

PL signals are derived mainly from oxygen vacancies and surface defects [47] and are based on the complexation of additional carriers, which is closely related to the density of material defects [35]. The introduction of oxygen vacancies can be reflected by the PL signals, which affect the PL peak intensity. The photoemission spectra have different intensities in the band range of 360–480 nm, among which the spectral intensities at wavelengths of 425 and 470 nm are relatively strong (Fig. 1(f)). Both peaks of Bi_2WO_{6-x}-2 are significantly stronger than those of Bi_2WO_6, indicating an increased density of oxygen vacancies [48]. The incorporation of oxygen vacancies can stimulate the recombination of charged carriers to a certain degree, ultimately resulting in increased PL emission intensity [49]. In addition, the incorporation of oxygen vacancy defects in the material can also affect the vibrational modes [35]. The Raman characteristic peaks of Bi_2WO_6 and Bi_2WO_{6-x}-2 are displayed (Fig. 1(g)). The strong peak at 796 cm^{-1} is attributed to the antisymmetric Ag stretching modes of the terminal O–W–O groups [41,50,51]. The peak at 715 cm^{-1} corresponds to the asymmetric stretching vibration between the W plane and O atoms [52]. The peak at 153 cm^{-1} originates from the external vibration of the WO_6 octahedron [41,52]. A slight redshift is observed in the peaks in the range of 87–550 cm^{-1} for Bi_2WO_{6-x}-2. All the other peaks at 170–520 cm^{-1} are attributed mainly to the stretching or bending vibrations of the WO_6 octahedron, BiO_6 polyhedron, and Bi–O bonds [52]. All the Raman peaks of Bi_2WO_{6-x}-2 are wider and weaker than those of Bi_2WO_6. These results ultimately indicate that the crystallinity and symmetry of Bi_2WO_{6-x}-2 decrease because some oxygen atoms are removed from Bi_2WO_6, resulting in the formation of oxygen vacancies [53].

The atomic chemical microenvironments of the as-prepared Bi_2WO_{6-x} samples were examined via XPS analysis (Fig. S7(a) in the ESM). In addition to the characteristic peaks ascribed to Bi, W, O, and C, no peaks corresponding to other elements can be observed (Figs. 1(h)–1(j) and Figs. S7(b)–S7(d) in the ESM). All the binding energies are calibrated using the binding energy of C 1s. On the basis of the Bi 4f spectra of Bi_2WO_6 and Bi_2WO_{6-x}-2 (Fig. 1(h)), the peaks of Bi_2WO_6 at 164.0 and 158.7 eV can be attributed to Bi $4f_{7/2}$ and Bi $4f_{5/2}$ spin–orbit splitting in the Bi^{3+} chemical state, respectively. Bi_2WO_{6-x}-2 demonstrates a 0.1 eV shift to a higher binding energy than Bi_2WO_6, owing to the formation of neighboring oxygen vacancies with higher electron-

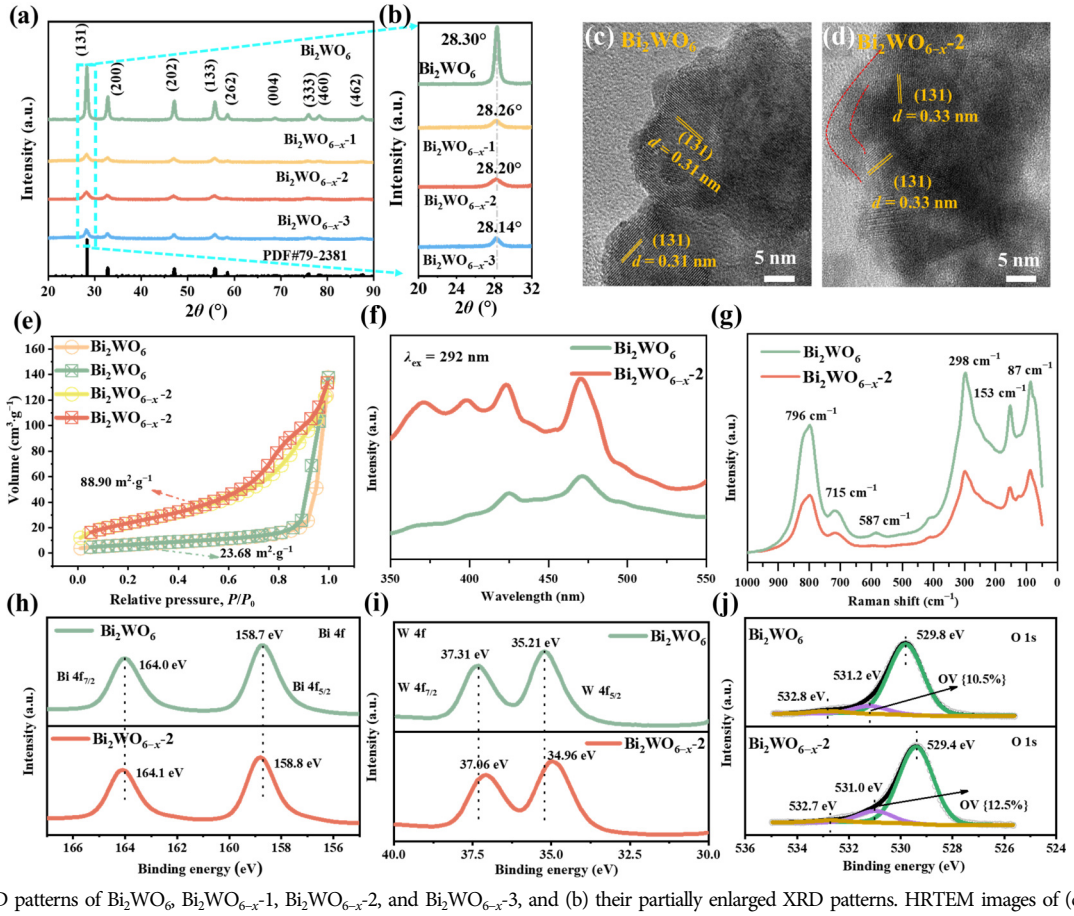

Fig. 1 (a) XRD patterns of Bi_2WO_6, Bi_2WO_{6-x}-1, Bi_2WO_{6-x}-2, and Bi_2WO_{6-x}-3, and (b) their partially enlarged XRD patterns. HRTEM images of (c) Bi_2WO_6 and (d) Bi_2WO_{6-x}-2. (e) N_2 adsorption/desorption isotherms of Bi_2WO_6 and Bi_2WO_{6-x}-2. (f) PL spectra and (g) Raman spectra of Bi_2WO_6 and Bi_2WO_{6-x}-2. (h–j) XPS Bi 4f, W 4f, and O 1s core spectra of Bi_2WO_6 and Bi_2WO_{6-x}-2, respectively.

attracting ability [41]. The opposite tendency is observed in the W 4f spectrum, which shifts to a lower binding energy (Fig. 1(i)). The above discussions suggest that the existence of oxygen vacancies increases the electron density around W^{6+} ions, thus decreasing the binding energy of W^{6+} ions [54,55]. Furthermore, a similar phenomenon of reduced binding energy is observed in the high-resolution O 1s spectra [56] (Fig. 1(j)). The asymmetric O 1s peak of Bi_2WO_6 can be deconvoluted into three peaks at 529.8, 531.2, and 532.8 eV, corresponding to lattice O, oxygen vacancies, and chemisorption of oxygen, respectively [57,58]. On the basis of the proportion of the oxygen vacancy peak area O 1s, Bi_2WO_{6-x}-2 has C_{OV} of 12.5%, which is higher than that of Bi_2WO_6 (10.4%) [57]. The successful introduction of oxygen vacancies will lay a foundation for subsequent research on the mechanism of piezocatalytic water splitting for hydrogen production.

In general, EPR can measure unpaired electrons such as O sites [59]. To further quantitatively determine the C_{OV} of the four samples, EPR spectroscopy was conducted (Figs. 2(a) and 2(b)). The EPR signal from Bi_2WO_6 did not obviously change, indicating that almost all the oxygen vacancies were effectively healed by the high-temperature annealing treatment. In addition, a gradually increased EPR signal of approximately g = 2.003 for Bi_2WO_6 and Bi_2WO_{6-x} can be attributed to the combination of electrons trapped in oxygen vacancies [34,53]. Figure 2(b) shows the calculated C_{OV} of the four samples according to the EPR spectra. C_{OV} increases significantly by 0.05×10^{12}, 0.97×10^{12}, 1.45×10^{12}, and 2.98×10^{12} spins·mg^{-1} for Bi_2WO_6, Bi_2WO_{6-x}-1, Bi_2WO_{6-x}-2, and Bi_2WO_{6-x}-3, respectively, which agrees well with the XRD results. From the samples of Bi_2WO_6, Bi_2WO_{6-x}-1 (180 °C for 12 h), and Bi_2WO_{6-x}-3 (180 °C for 20 h), it can be inferred that the longer the solvothermal time is, the greater the concentration of oxygen vacancies produced. From the samples of Bi_2WO_6, Bi_2WO_{6-x}-2 (160 °C for 20 h), and Bi_2WO_{6-x}-3 (180 °C for 20 h), it can be inferred that the higher the solvothermal temperature is, the greater the concentration of oxygen vacancies produced.

Generally, piezoelectric performance is a nonnegligible element of the piezocatalytic activity of samples. To further investigate the effect of oxygen vacancies on the piezoelectric performance of materials, PFM measurements were performed. (Figs. 2(c) and 2(d) and Figs. S8(a) and S8(b) in the ESM). As presented in the typical amplitude–voltage butterfly loops, a ±12 V DC bias field was applied, illustrating the existence of a local piezoelectric field. According to the amplitude–voltage butterfly loops, the effective piezoelectric coefficient (d^*_{33}) values of Bi_2WO_6, Bi_2WO_{6-x}-1, Bi_2WO_{6-x}-2, and Bi_2WO_{6-x}-3 can be calculated as 16.9, 15.2, 13.9, and 13.5 pm·V^{-1}, respectively (Fig. 2(e)). Therefore, the relationship between d^*_{33} and C_{OV} can be described in Fig. 2(f). With increasing C_{OV}, d^*_{33} of the sample decreases. This is due to the following two reasons. First, the construction of oxygen vacancies leads to the aging of the material and a decrease in domain wall mobility due to the domain wall pinning effect, which weakens the piezoresponse of the material [60,61]. Second, the introduction of oxygen vacancies increases the carrier concentration of materials, which can enhance the screening effect to hinder polarization reversal behavior, thereby adversely affecting the material's piezoelectricity [21,62]. In regard to

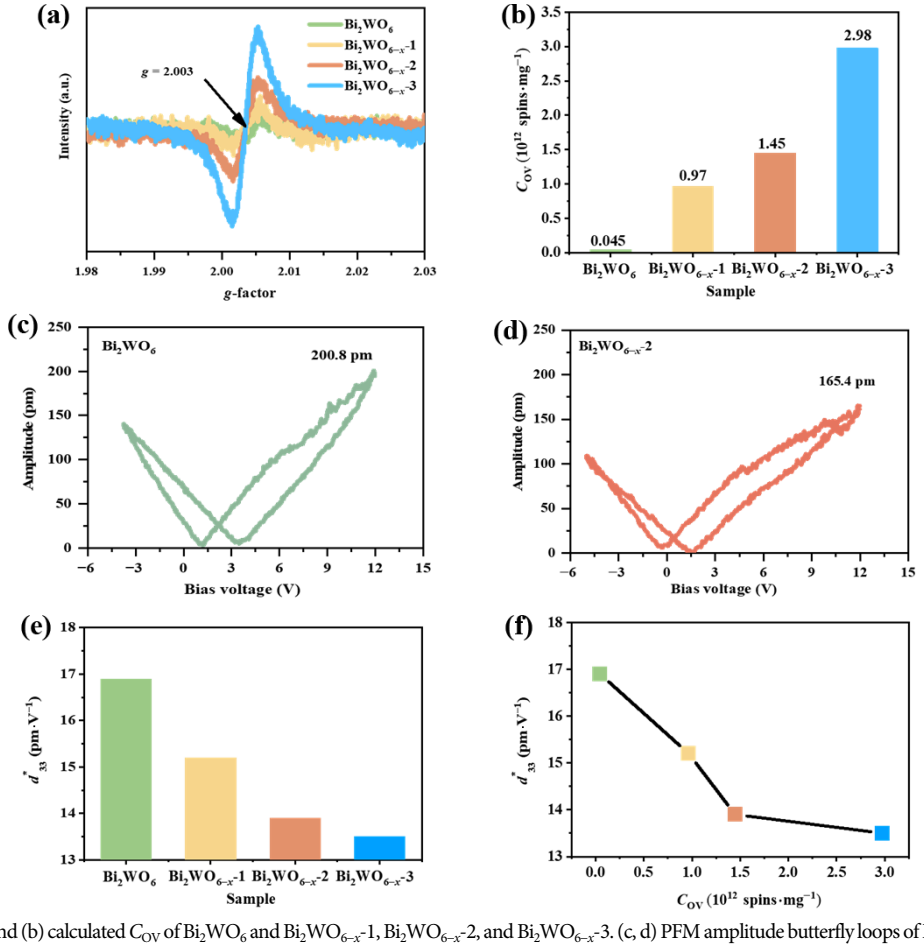

Fig. 2 (a) EPR spectra and (b) calculated C_{OV} of Bi_2WO_6 and Bi_2WO_{6-x}-1, Bi_2WO_{6-x}-2, and Bi_2WO_{6-x}-3. (c, d) PFM amplitude butterfly loops of Bi_2WO_6 and Bi_2WO_{6-x}-2. (e) Calculation of piezoelectric coefficients of Bi_2WO_{6-x} samples. (f) Relationship between piezoelectric coefficient and C_{OV}.

centrosymmetric materials or ferroelectric materials, which do not exhibit ferroelectric performance at room temperature, introducing atomic defects [63] or asymmetric centers through nonstoichiometric engineering [64] can, in contrast, build piezoelectric/ferroelectricity. Wang *et al.* [65] realized the piezoelectric response of $SrFeO_3$ through enhancing its centrosymmetric breaking by introducing oxygen vacancies.

The electrical properties of the Bi_2WO_{6-x} samples with and without oxygen vacancies were measured through Mott-Schottky curves (Fig. 3(a)). N_d under different reaction conditions can be determined according to Eq. (2) [66]:

$$N_d = \left(\frac{2}{e_0 \varepsilon_0 \varepsilon}\right)\left[\frac{d\left(1/C^2\right)}{dV}\right]^{-1} \quad (2)$$

where e_0, ε_0, and ε represent the electronic charge unit (1.6×10^{19} C), the vacuum permittivity (8.85×10^{14} F·m^{-1}), and the dielectric constant of the materials, respectively [67]. C and V are capacitance and voltage. $1/C^2$ and V are the vertical and horizontal coordinates of the Mott-Schottky curves. $d(1/C^2)/dV$ is the slope of the Mott-Schottky plot. Generally, the smaller the slope of the Mott-Schottky plot is, the greater the N_d [68–70]. The N_d values of Bi_2WO_6, Bi_2WO_{6-x}-1, Bi_2WO_{6-x}-2, and Bi_2WO_{6-x}-3 are calculated as 1.97×10^{20}, 2.63×10^{20}, 2.90×10^{20}, and 4.11×10^{20} cm^{-3}, respectively, which show a linear trend with increasing C_{OV} (Fig. 3(b)). Oxygen vacancies can generate free electrons or holes in a material depending on the chemical stoichiometry and electronic structure of the material [29]. In metal oxides, oxygen vacancies usually carry a positive charge because when the oxygen atoms in the lattice leave, two electrons that originally belong to other atoms are removed, forming a positively charged defect [71]. This positively charged defect can attract electrons, thereby increasing the electron concentration of the material, which in turn increases the carrier concentration [68,72]. Moreover, oxygen vacancies introduce additional energy level states in the band structure, which can serve as centers for the generation or recombination of charge carriers. Under appropriate conditions, these energy levels can serve as traps for electrons or holes, thereby increasing the carrier concentration of the material [24,25].

The carrier separation and transfer efficiency of the samples were further investigated via EIS (Fig. 3(c)) and the transient piezocurrent response (Fig. 3(d)). The semicircular arc of the Nyquist diagram reflects the charge transfer dynamics of the electrode [73]. The smaller curvature radius of the impedance arc of Bi_2WO_{6-x}-2 than that of Bi_2WO_6 indicates a smaller interfacial resistance and stronger charge transfer efficiency (Fig. 3(c)). Oxygen vacancy defects can significantly alleviate the low conductivity and high charge transfer resistance of Bi_2WO_6 [55]. The piezocurrent results indicate that both Bi_2WO_6 and Bi_2WO_{6-x}-2 exhibit sensitive piezoresponses under vibration, and when the vibration is turned off, the piezocurrent decreases sharply (Fig. 3(d)). Additionally, Bi_2WO_{6-x}-2 has a larger piezocurrent value than Bi_2WO_6 does because of efficient carrier separation and transfer. As depicted above, the introduction of oxygen vacancies further increases the piezocurrent density due to the efficient enhancement of carrier transferability [55].

3.2 Piezocatalytic water splitting for hydrogen generation

To better test the effect of oxygen vacancy on piezocatalytic performance, a series of piezocatalytic water splitting experiments were conducted on as-synthesized Bi_2WO_{6-x}. As shown in Fig. 4(a), it can be observed that the overall hydrogen production shows a volcanic pattern with the increase of C_{OV}, and Bi_2WO_{6-x}-2 behaves with the best average hydrogen production efficiency of ~157 μmol·g^{-1}·h^{-1}. However, with a further increase in C_{OV}, Bi_2WO_{6-x}-3 has the lowest average hydrogen production rate of ~20 μmol·g^{-1}·h^{-1}. The introduction of oxygen vacancies at certain concentrations can effectively promote carrier transport; however, when the C_{OV} is too high, it becomes a trapping center and leads to charge recombination [74]. Therefore, an optimal C_{OV} has more advantages and fewer drawbacks for catalytic performance.

In addition to the solvothermal time and temperature, the annealing time can also regulate the C_{OV}, thus affecting the

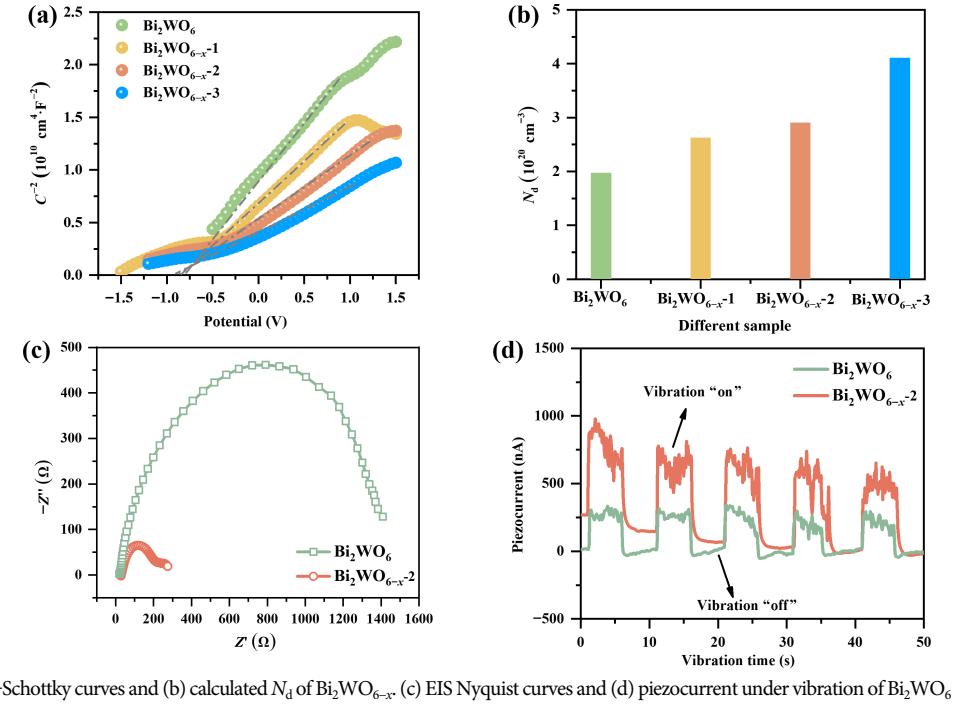

Fig. 3 (a) Mott-Schottky curves and (b) calculated N_d of Bi_2WO_{6-x}. (c) EIS Nyquist curves and (d) piezocurrent under vibration of Bi_2WO_6 and Bi_2WO_{6-x}-2.

piezocatalytic hydrogen production efficiency. To obtain a more obvious comparative effect, Bi_2WO_{6-x}-3, with the largest C_{OV} of 2.98×10^{12} spins·mg^{-1} was selected as the experimental object to study the influence of the annealing time and C_{OV} on the catalytic performance. As shown in Figs. 4(b)–4(d), with increasing annealing time, C_{OV} of Bi_2WO_{6-x}-3 decreases gradually, and hydrogen production reaches its highest value at an annealing time of 2 h. When the annealing time reaches 4 and 6 h, the EPR signal intensity remains almost unchanged, suggesting that the oxygen vacancies are nearly filled after 4 h of annealing; therefore, hydrogen production also reaches a stable value. The excess oxygen vacancies can be oxidized during annealing in air, achieving a state of C_{OV} equilibrium, which is conducive to improving the efficiency of piezocatalytic hydrogen production. However, with increasing annealing time, the C_{OV} decreases, and the role of the oxygen vacancy as the active site can be ignored, which inevitably affects the piezocatalytic activity.

In addition, the piezoelectric coefficient (d_{33}) and the extra mechanical pressure (T) affect the quantity of piezoelectric charges (q) in piezoelectric materials ($q = d_{33}T$) [75]. As ultrasonic stress plays a crucial role in piezocatalysis, increasing power can assign more mechanical energy to piezocatalysts, exciting a stronger piezoelectric potential in the whole reaction to trigger more active electric charges and hinder charge recombination [76,77]. As presented in Fig. 4(e), with increasing applied vibration power from 60 to 100 W, the performance of the piezocatalytic hydrogen production rate increases gradually, reaching ~221 μmol·g^{-1}·h^{-1} at 100 W. A comparison of the hydrogen production rates of other reported piezocatalysts under different conditions and strategies is shown in Table S1 in the ESM, the hydrogen production rate per power of 2.21 μmol·g^{-1}·h^{-1}·W^{-1} is equivalent to or even better than that of most reported piezocatalysts.

To further understand the effects of (piezoelectrically active charges and catalysts in generating H_2, the following series of comparative experiments were carried out. In the case of water and MeOH, only a small amount of hydrogen is produced, which can be negligible (Fig. 4(f)). In the presence of catalyst and water, the hydrogen production rate increases slightly but not significantly, which is mainly due to the rapid recombination of piezo-induced q^+ and q^-. When MeOH is added to the reaction mixture as a sacrificial agent, a part of the piezoelectric q^+ is captured, and more unrecombined negative charges react with H^+ to produce more hydrogen. In addition, XRD analysis of Bi_2WO_6 and Bi_2WO_{6-x}-2 before and after the reaction was performed to explore the crystal structure stability (Fig. S9 in the ESM). After the reaction, all the characteristic peaks of Bi_2WO_6 and Bi_2WO_{6-x}-2 remain unchanged from those before the reaction (PDF#79-2381), indicating the strong crystal structure stability of both samples. However, both intensities of the diffraction peaks of the samples weaken slightly after the reaction, which can be caused by the decreased crystallinity of the catalyst after ultrasonic vibration. An EPR test was subsequently performed on Bi_2WO_{6-x}-2 after the reaction to explore the stability of the oxygen vacancies. After the reaction, a relatively weaker oxygen vacancy signal of Bi_2WO_{6-x}-2 appears (Fig. S10 in the ESM), suggesting a reduced concentration of oxygen vacancies, which could be caused by oxidation and occupation by various reactant molecules, leading to deactivation of the oxygen vacancies [78–80]. The deactivation of oxygen vacancies also leads to poor catalytic stability over several cycles (Fig. S11 in the ESM). In the future, maintaining the stability of oxygen vacancies may also be an issue that needs attention.

3.3 Piezocatalytic mechanism exploration

To the best of our knowledge, the energy level distribution of catalysts is particularly important for investigating the piezocatalytic reaction mechanism. UV–Vis diffuse reflectance spectra of Bi_2WO_6 (yellowish white in color) and Bi_2WO_{6-x}-2 (gray in color) were measured to obtain band gap information (Fig. 5(a)). By tangential to the absorption spectra, the point of intersection with the horizontal coordinate is the absorption limit of the wavelength. The absorption at the edge of the band can be expressed by Eq. (3) [76,81]:

$$(ahv)^{1/2} = A(hv - E_g) \quad (3)$$

where α, h, v, A, and E_g refer to the absorption coefficient, the Planck's constant, the frequency of the irradiated light, a constant, and the bandgap, respectively. Hence, by plotting $(ahv)^2$–hv and making tangential lines, E_g values of Bi_2WO_6 and Bi_2WO_{6-x}-2 of

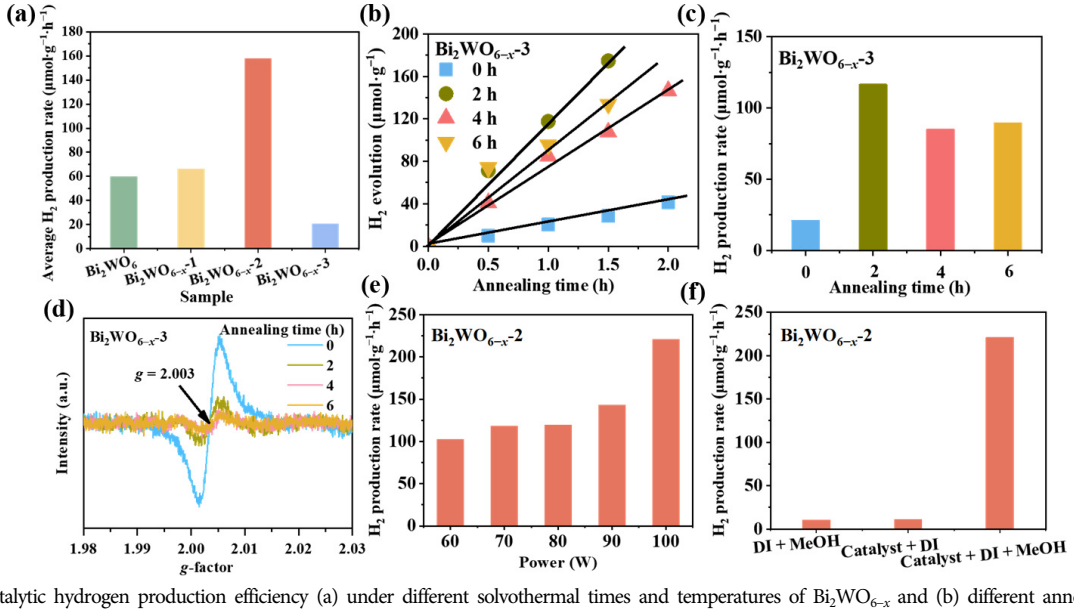

Fig. 4 Piezocatalytic hydrogen production efficiency (a) under different solvothermal times and temperatures of Bi_2WO_{6-x} and (b) different annealing times of Bi_2WO_{6-x}-3. (c) H_2 production rates of Bi_2WO_{6-x}-3 after different annealing times. (d) EPR signal of Bi_2WO_{6-x}-3 after annealing for 0, 2, 4, and 6 h. Hydrogen production rates of Bi_2WO_{6-x}-2 (e) under different ultrasonic powers and (f) with and without MeOH.

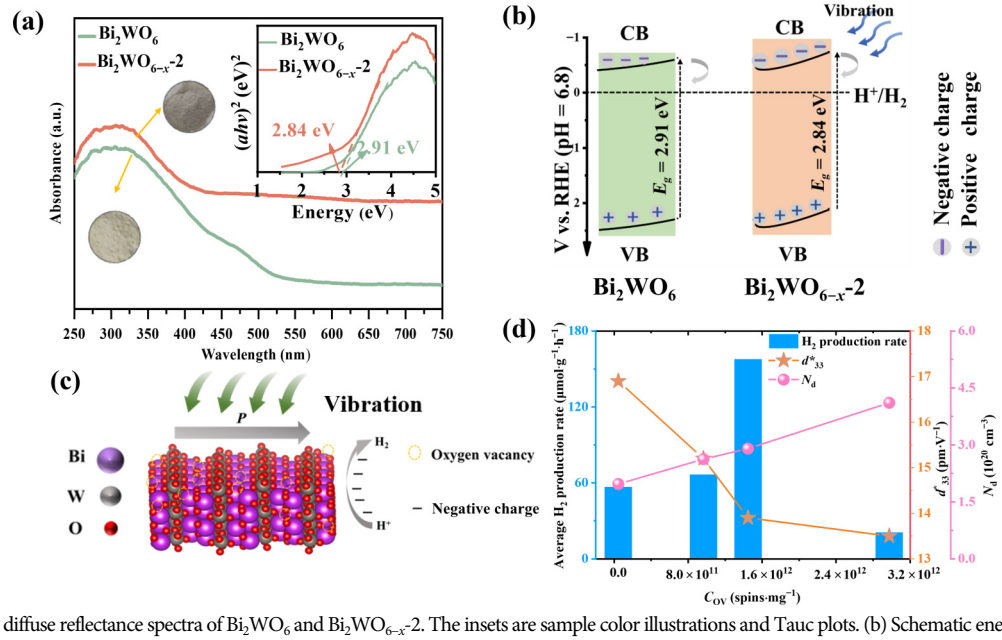

Fig. 5 (a) UV–Vis diffuse reflectance spectra of Bi_2WO_6 and Bi_2WO_{6-x}-2. The insets are sample color illustrations and Tauc plots. (b) Schematic energy levels of Bi_2WO_6 and Bi_2WO_{6-x}-2. (c) Schematic illustration of piezocatalytic hydrogen generation. (d) Relationships between d^*_{33}, N_d, and piezocatalytic performance as a function of C_{OV}.

2.91 and 2.85 eV can be obtained (the inset of Fig. 5(a)). Obviously, E_g of Bi_2WO_{6-x}-2 is smaller than that of Bi_2WO_6. Defect engineering is one of the most effective strategies for reducing the bandgap width, among which the use of oxygen vacancies is one of the simplest methods. The phenomenon of oxygen vacancy-induced band gap narrowing has also been confirmed by other researchers [82–84]. The introduced defects can produce new energy levels in the band gap, which can act as traps or donors for electrons, forming freely moving charge carriers or providing additional transition paths for electrons, thus narrowing the band gap width [24,25].

In addition, Mott-Schottky curves were also measured to determine the flat band energy (E_f) of the materials (Fig. 3(a)). The measured E_f values of Bi_2WO_6 and Bi_2WO_{6-x}-2 are −0.816 and −0.873 V vs. SCE, respectively. The reversible hydrogen electrode (RHE) potential ($E_{f,RHE}$) can be measured as Eq. (4) [85]:

$$E_{f,RHE} = E_{f,SCE} + (0.0591 \times pH + 0.24)\ (V) \quad (4)$$

where the pH value of the Na_2SO_4 electrolyte is 6.8. The calculated $E_{f,RHE}$ values of Bi_2WO_6 and Bi_2WO_{6-x}-2 are −0.174 and −0.231 V vs. RHE (pH = 6.8), respectively. The results can also be proven by the surface function of the materials through KPFM (Figs. S12(a)–S12(f) in the ESM). The average surface contact potential difference (CPD) value of Bi_2WO_{6-x} (~407.98 mV) is lower than that of Bi_2WO_6 (~928.21 mV). The work function φ of the samples can be determined via Eq. (5) [86,87]:

$$\frac{\varphi_{tip} + \varphi_{sample}}{e} = V_{CPD} \quad (5)$$

where V_{CPD} is CPD between the tip and sample; φ_{tip} and φ_{sample} are the work functions of the tip and the sample, respectively; and e represents the elementary charge. A lower CPD value results in a reduced surface work function. The work function can be expressed as the difference between the vacuum level and the Fermi level. The smaller the work function is, the more negative the Fermi level is at the energy band position.

The positive slope indicates that Bi_2WO_6 is an n-type semiconductor [88]. The reported $E_{f,RHE}$ is approximately 0.3 V below the minimum CB for typical n-type semiconductors [89]. Hence, the CB potentials of Bi_2WO_6 and Bi_2WO_{6-x} are −0.474 and −0.531 V, respectively. Moreover, the CB level of H^+/H_2 (pH = 7.0) is approximately −0.01 V vs. RHE (pH = 6.8), and the energy band positions of Bi_2WO_6 and Bi_2WO_{6-x}-2 support H^+ reduction into H_2 [90]. Simultaneously, according to Eq. (6) [81],

$$E_g = E_{VB} - E_{CB} \quad (6)$$

The valence band (VB) potentials of Bi_2WO_6 and Bi_2WO_{6-x} are calculated as 2.436 and 2.319 V, respectively. According to band tilt theory, the detailed energy band positions of Bi_2WO_6 and Bi_2WO_{6-x}-2 are shown in Fig. 5(b) [91,92]. Obviously, the CB of Bi_2WO_{6-x}-2 after oxygen vacancy regulation is more negative than that of Bi_2WO_6, resulting in more efficient hydrogen production.

On the basis of the above analysis, a possible mechanism of piezocatalytic hydrogen production over Bi_2WO_{6-x} is illustrated clearly in Fig. 5(c). With the exertion of external ultrasonic vibration, Bi_2WO_{6-x} is obliged to deform, inducing sufficient piezoinduced q^+ and q^- electric charges.

$$Bi_2WO_{6-x} \xrightarrow{Vibration} Bi_2WO_{6-x} + q^+ + q^- \quad (7)$$

The piezoinduced q^+ and q^- electric charges are separated and migrated to the opposite surfaces of Bi_2WO_{6-x}, thereby establishing an internal polarized electric field over the entire piezoelectric body. The intrinsic polarization of Bi_2WO_{6-x} is considered to be the main driving force during the piezocatalytic process, which can trigger the tilting of their energy bands and thus drive the active q^- to perform hydrogen evolution Eq. (8) [90].

$$2H^+ + 2q^- \rightarrow H_2 \quad (8)$$

The piezoinduced q^+ is consumed by MeOH to form H^+ and hydroxyalkyl radical intermediates ($\cdot CH_2OH$). Moreover, the presence of oxygen vacancies on Bi_2WO_{6-x} can also offer more active sites for the catalytic reaction, accelerate the H^+ reduction reaction, and thus increase the hydrogen production rate.

A correlation diagram of the piezoelectric coefficient, carrier concentration, and piezocatalytic performance can be drawn (Fig. 5(d)). As C_{OV} increases from 0.05×10¹² to 2.98×10¹² spins·mg⁻¹,

d^*_{33} decreases from 16.9 to 13.5 pm·V^{-1}, N_d increases from 1.97×10^{20} to 4.11×10^{20} cm^{-3}, and the hydrogen production rate first increases and then decreases, with the best effect observed in Bi_2WO_{6-x}-2. Although the introduction of oxygen vacancies weakens the piezoelectric response of Bi_2WO_6 due to the domain wall pinning effect [60,61] and the screening effect [21,62], the carrier concentration of materials increases instead [93]. The inverse relationship between the carrier concentration and piezoelectric output performance is also applicable in nonferroelectric piezoelectric materials, such as ZnO [94]. When the C_{OV} increases from 8.0×10^{11} to 1.6×10^{12}, d^*_{33} significantly decreases, whereas N_d only slightly increases; however, the hydrogen production still increases substantially. Some other factors that may affect catalytic performance. Zhao *et al.* [22] compared the efficiency of piezocatalytic dye decomposition via the high-conductivity piezoelectric material $Bi_{0.5}Na_{0.5}TiO_3$ (conductivity of 10^{-5} S·m^{-1}) and reported that conductivity has a greater impact than the piezoelectric coefficient on piezocatalytic activity. Moreover, researchers in the field of electrocatalysis reported the crucial role of surface oxygen vacancies in enhancing electron transport, reducing the charge transfer resistance by more than an order of magnitude [95]. In addition, the ultrasonic cavitation effect causes small cavitation bubbles to rupture and can form a piezoelectric potential on the local surface of the material, thereby affecting the migration efficiency of charge carriers [96–98]. Factors affecting the efficiency of the ultrasonic cavitation effect include the ultrasonic frequency, dissolved gas, ultrasonic power, and water temperature [99,100].

When the concentration of oxygen vacancies reaches 1.45×10^{12} spins·mg^{-1}, the corresponding piezoelectric coefficient and carrier concentration values are 13.90 pm·V^{-1} and 2.90×10^{20} cm^{-3}, respectively. The optimal hydrogen production rate per power of 2.21 μmol·g^{-1}·h^{-1}·W^{-1} is equivalent to or even better than that of most reported piezocatalysts. In the catalytic reaction, the number of carriers plays a decisive role in the catalytic efficiency. However, an excess number of carriers may become trapping centers and lead to charge recombination [74]. Therefore, only a medium C_{OV} can obtain an appropriately elevated carrier concentration and effectively offset the negative effects caused by a reduction in the piezoelectric coefficient. The piezoelectric coefficient and carrier concentration, as two factors, jointly determine the piezocatalytic performance.

4 Conclusions

In this work, the piezoelectric coefficient and carrier concentration of Bi_2WO_6 were adjusted by introducing oxygen vacancies, and the corresponding effects on the performance of piezocatalytic hydrogen generation were studied. Although increasing C_{OV} inhibits d^*_{33}, it increases N_d inverse, and the hydrogen production rate exhibits a volcanic pattern. The piezoelectric coefficient and carrier concentration, as two factors, jointly determine the piezocatalytic performance. The optimal hydrogen production rate per power of 2.21 μmol·g^{-1}·h^{-1}·W^{-1} is equivalent to or even better than that of most reported piezocatalysts. This work not only offers technical and mechanistic support for the research and application of oxygen vacancy defect engineering but also provides a scientific reference for the exploration of additional excellent piezocatalytic materials in the future.

Acknowledgements

This work was supported by the National Natural Science Foundation of China (Nos. 22309170, 51972294, and 51972291), the Natural Science Foundation of Zhejiang Province (No. LQ24E020003), and the Open Fund Project of the National-Local Joint Engineering Research Center of Heavy Metals Pollutants Control and Resource Utilization of Nanchang Hangkong University (No. ES202480182). The authors extend their gratitude to the Shiyanjia Lab (www.shiyanjia.com) for providing invaluable assistance with the material characterization analysis.

Declaration of competing interest

The authors have no competing interests to declare that are relevant to the content of this article.

Electronic Supplementary Material

Supporting material is available in the online version of this article at https://doi.org/10.26599/JAC.2024.9220970.

References

[1] Long Y, Xu H, He J, *et al.* Piezoelectric polarization of BiOCl via capturing mechanical energy for catalytic H_2 evolution. *Surf Interfaces* 2022, **31**: 102056.
[2] Li S, Zhang XY, Yang F, *et al.* Mechanically driven water splitting over piezoelectric nanomaterials. *Chem Catal* 2024, **4**: 100901.
[3] Ji WQ, Zhang K, Zhan K, *et al.* Solar-powered environmentally friendly hydrogen production: Advanced technologies for sunlight–electricity–hydrogen nexus. *Chin J Struct Chem* 2022, **41**: 2205015–2205029.
[4] Zhao G, Ma WX, Wang XK, *et al.* Self-water-absorption-type two-dimensional composite photocatalyst with high-efficiency water absorption and overall water-splitting performance. *Adv Powder Mater* 2022, **1**: 100008.
[5] Shang WZ, Liu W, Cai XB, *et al.* Insights into atomically dispersed reactive centers on g-C_3N_4 photocatalysts for water splitting. *Adv Powder Mater* 2023, **2**: 100094.
[6] Feng WH, Yuan J, Gao F, *et al.* Piezopotential-driven simulated electrocatalytic nanosystem of ultrasmall MoC quantum dots encapsulated in ultrathin N-doped graphene vesicles for superhigh H_2 production from pure water. *Nano Energy* 2020, **75**: 104990.
[7] He TF, Cao ZZ, Li GR, *et al.* High efficiently harvesting visible light and vibration energy in $(1-x)AgNbO_{3-x}LiTaO_3$ solid solution around antiferroelectric–ferroelectric phase boundary for dye degradation. *J Adv Ceram* 2022, **11**: 1641–1653.
[8] Li Z, Lan SY, Zhu MS. Piezoelectricity activates persulfate for water treatment: A perspective. *Environ Sci Ecotechnol* 2024, **18**: 100329.
[9] Bao YP, Xiao KK, Yue S, *et al.* Wastewater decontamination via piezoelectric based technologies: Materials design, applications and prospects. *Surf Interfaces* 2023, **40**: 103107.
[10] Li S, Zhao ZC, Yu DF, *et al.* Few-layer transition metal dichalcogenides (MoS_2, WS_2, and WSe_2) for water splitting and degradation of organic pollutants: Understanding the piezocatalytic effect. *Nano Energy* 2019, **66**: 104083.
[11] Yu CY, Tan MX, Tao CD, *et al.* Remarkably enhanced piezo-photocatalytic performance in $BaTiO_3$/CuO heterostructures for organic pollutant degradation. *J Adv Ceram* 2022, **11**: 414–426.
[12] Yan XH, Li G, Wang ZY, *et al.* Recent progress on piezoelectric materials for renewable energy conversion. *Nano Energy* 2020, **77**: 105180.
[13] Li T, Hu WJ, Tang CX, *et al.* Enhanced piezo-catalysis in ZnO rods with built-in nanopores. *J Adv Ceram* 2023, **12**: 2271–2283.
[14] Jia YM, Wang XX, Zhang QC, *et al.* Research progress in enhancement strategies and mechanisms of piezo–electro–chemical coupling. *Acta Phys Sin-Ch Ed* 2023, **72**: 087701.
[15] Phuong PTT, Vo DV N, Duy NPH, *et al.* Piezoelectric catalysis for efficient reduction of CO_2 using lead-free ferroelectric particulates. *Nano Energy* 2022, **95**: 107032.
[16] Li S, Zhao ZC, Liu MS, *et al.* Remarkably enhanced photocatalytic performance of Au/$AgNbO_3$ heterostructures by coupling piezotronic with plasmonic effects. *Nano Energy* 2022, **95**: 107031.

[17] Su R, Hsain HA, Wu M, *et al.* Nano-ferroelectric for high efficiency overall water splitting under ultrasonic vibration. *Angew Chem Int Edit* 2019, **58**: 15076–15081.
[18] Bößl F, Tudela I. Piezocatalysis: Can catalysts really dance. *Curr Opin Green Sustain Chem* 2021, **32**: 100537.
[19] Yuan BW, Wu J, Qin N, *et al.* Sm-doped $Pb(Mg_{1/3}Nb_{2/3})O_{3-x}PbTiO_3$ piezocatalyst: Exploring the relationship between piezoelectric property and piezocatalytic activity. *Appl Mater Today* 2019, **17**: 183–192.
[20] Sun XX, Li RC, Yang ZW, *et al.* Modulating polarization rotation to stimulate the high piezocatalytic activity of (K,Na)NbO_3 lead-free piezoelectric materials. *Appl Catal B-Environ* 2022, **313**: 121471.
[21] Ji M, Kim JH, Ryu CH, *et al.* Synthesis of self-modified black $BaTiO_{3-x}$ nanoparticles and effect of oxygen vacancy for the expansion of piezocatalytic application. *Nano Energy* 2022, **95**: 106993.
[22] Zhao ZC, Wei LY, Li S, *et al.* Exclusive enhancement of catalytic activity in $Bi_{0.5}Na_{0.5}TiO_3$ nanostructures: New insights into the design of efficient piezocatalysts and piezo-photocatalysts. *J Mater Chem A* 2020, **8**: 16238–16245.
[23] Li S, Zhao ZC, Li JB, *et al.* Mechanically induced highly efficient hydrogen evolution from water over piezoelectric SnSe nanosheets. *Small* 2022, **18**: 2202507.
[24] Dong W, Xiao HY, Jia YM, *et al.* Engineering the defects and microstructures in ferroelectrics for enhanced/novel properties: An emerging way to cope with energy crisis and environmental pollution. *Adv Sci* 2022, **9**: 2105368.
[25] Liao JY, Lv X, Sun XX, *et al.* Boosting piezo-catalytic activity of KNN-based materials with phase boundary and defect engineering. *Adv Funct Mater* 2023, **33**: 2303637.
[26] Yuan J, Feng WH, Zhang YF, *et al.* Unraveling synergistic effect of defects and piezoelectric field in breakthrough piezo-photocatalytic N_2 reduction. *Adv Mater* 2024, **36**: 2303845.
[27] Zhong WJ, Hung MY, Kuo YT, *et al.* Dual-vacancy-engineered $ZnIn_2S_4$ nanosheets for harnessing low-frequency vibration induced piezoelectric polarization coupled with static dipole field to enhance photocatalytic H_2 evolution. *Adv Mater* 2024, **36**: 2403228.
[28] Yu HJ, Li JY, Zhang YH, *et al.* Three-in-one oxygen vacancies: Whole visible-spectrum absorption, efficient charge separation, and surface site activation for robust CO_2 photoreduction. *Angew Chem Int Edit* 2019, **58**: 3880–3884.
[29] Wang YC, Wu JM. Effect of controlled oxygen vacancy on H_2-production through the piezocatalysis and piezophototronics of ferroelectric R_3C $ZnSnO_3$ nanowires. *Adv Funct Mater* 2020, **30**: 1907619.
[30] Liu XT, Gu SN, Zhao YJ, *et al.* $BiVO_4$, Bi_2WO_6 and Bi_2MoO_6 photocatalysis: A brief review. *J Mater Sci Technol* 2020, **56**: 45–68.
[31] Elaouni A, El Ouardi M, BaQais A, *et al.* Bismuth tungstate Bi_2WO_6: A review on structural, photophysical and photocatalytic properties. *RSC Adv* 2023, **13**: 17476–17494.
[32] Xu XL, Xiao LB, Wu Z, *et al.* Harvesting vibration energy to piezo-catalytically generate hydrogen through Bi_2WO_6 layered-perovskite. *Nano Energy* 2020, **78**: 105351.
[33] Liu MY, Wan YY, Wang Y, *et al.* Robust photoelectrocatalytic degradation of antibiotics by organic–inorganic PDISA/Bi_2WO_6 S-scheme heterojunction membrane. *J Environ Chem Eng* 2024, **12**: 112328.
[34] Wang PL, Li XY, Fan SY, *et al.* Impact of oxygen vacancy occupancy on piezo-catalytic activity of $BaTiO_3$ nanobelt. *Appl Catal B-Environ* 2020, **279**: 119340.
[35] Zhao SH, Yang Y, Bi FK, *et al.* Oxygen vacancies in the catalyst: Efficient degradation of gaseous pollutants. *Chem Eng J* 2023, **454**: 140376.
[36] Jin JT, Liu YC, Zhao XD, *et al.* Annealing in argon universally upgrades the Na-storage performance of Mn-based layered oxide cathodes by creating bulk oxygen vacancies. *Angew Chem Int Edit* 2023, **62**: e202219230.
[37] Li H, Shi JG, Zhao K, *et al.* Sustainable molecular oxygen activation with oxygen vacancies on the {001} facets of BiOCl nanosheets under solar light. *Nanoscale* 2014, **6**: 14168–14173.
[38] Vengrenovych RD, Ivanskyy BV, Panko II, *et al.* Stability of nanocrystals in 2D and 3D systems in Ostwald ripening. *Powder Metall Met C+* 2015, **54**: 281–291.
[39] Gurusamy L, Karuppasamy L, Anandan S, *et al.* Review of oxygen-vacancies nanomaterials for non-enzymatic electrochemical sensors application. *Coordin Chem Rev* 2023, **484**: 215102.
[40] Ou G, Xu YS, Wen B, *et al.* Tuning defects in oxides at room temperature by lithium reduction. *Nat Commun* 2018, **9**: 1302.
[41] Kong XY, Choo YY, Chai SP, *et al.* Oxygen vacancy induced Bi_2WO_6 for the realization of photocatalytic CO_2 reduction over the full solar spectrum: From the UV to the NIR region. *Chem Commun* 2016, **52**: 14242–14245.
[42] Chen SS, Takata T, Domen K. Particulate photocatalysts for overall water splitting. *Nat Rev Mater* 2017, **2**: 17050.
[43] Wang TY, Feng CT, Liu JQ, *et al.* Bi_2WO_6 hollow microspheres with high specific surface area and oxygen vacancies for efficient photocatalysis N_2 fixation. *Chem Eng J* 2021, **414**: 128827.
[44] Porwal C, Gaur A, Chauhan VS, *et al.* Enhancing piezocatalytic dye degradation through ball milling-induced polarization in nano bismuth zinc borate. *Surf Interfaces* 2023, **42**: 103391.
[45] Jia BB, Liu G, Zhang BH, *et al.* General modification strategy on amorphous materials to boost catalytic performance. *Adv Funct Mater* 2024, **34**: 2405867.
[46] Hu XS, Li Y, Wei XX, *et al.* Preparation of double-layered Co–Ci/NiFeOOH co-catalyst for highly meliorated PEC performance in water splitting. *Adv Powder Mater* 2022, **1**: 100024.
[47] Jing LQ, Qu YC, Wang BQ, *et al.* Review of photoluminescence performance of nano-sized semiconductor materials and its relationships with photocatalytic activity. *Sol Energy Mat Sol C* 2006, **90**: 1773–1787.
[48] Tu N, Van Bui H, Trung DQ, *et al.* Surface oxygen vacancies of ZnO: A facile fabrication method and their contribution to the photoluminescence. *J Alloys Compd* 2019, **791**: 722–729.
[49] Liu Y, Wang WM, Fu ZY, *et al.* Nest-like structures of Sr doped Bi_2WO_6: Synthesis and enhanced photocatalytic properties. *Mater Sci Eng B-Adv* 2011, **176**: 1264–1270.
[50] Zhang LW, Wang YJ, Cheng HY, *et al.* Synthesis of porous Bi_2WO_6 thin films as efficient visible-light-active photocatalysts. *Adv Mater* 2009, **21**: 1286–1290.
[51] Crane M, Frost RL, Williams PA, *et al.* Raman spectroscopy of the molybdate minerals chillagite (tungsteinian wulfenite-I4), stolzite, scheelite, wolframite and wulfenite. *J Raman Spectrosc* 2002, **33**: 62–66.
[52] Wang WJ, Guo MN, Lu DL, *et al.* Effect of HNO_3 concentration on the morphologies and properties of Bi_2WO_6 photocatalyst synthesized by a hydrothermal method. *Crystals* 2016, **6**: 75.
[53] Lv YH, Liu YF, Zhu YY, *et al.* Surface oxygen vacancy induced photocatalytic performance enhancement of a $BiPO_4$ nanorod. *J Mater Chem A* 2014, **2**: 1174–1182.
[54] Zhang G, Hu ZY, Sun M, *et al.* Formation of Bi_2WO_6 bipyramids with vacancy pairs for enhanced solar-driven photoactivity. *Adv Funct Mater* 2015, **25**: 3726–3734.
[55] Kang ZH, Chen MS, Wu J, *et al.* Insights on enhancing piezocatalytic performance of Bi_2WO_6@PDA homojunction from phase coexistence and electron transfer mediators. *J Colloid Interf Sci* 2023, **650**: 169–181.
[56] Lv YH, Yao WQ, Zong RL, *et al.* Fabrication of wide-range-visible photocatalyst Bi_2WO_{6-x} nanoplates via surface oxygen vacancies. *Sci Rep* 2016, **6**: 19347.
[57] Dai J, Shao NN, Zhang SW, *et al.* Enhanced piezocatalytic activity of $Sr_{0.5}Ba_{0.5}Nb_2O_6$ nanostructures by engineering surface oxygen vacancies and self-generated heterojunctions. *ACS Appl Mater Inter* 2021, **13**: 7259–7267.
[58] Xue KL, Jiang Y, Mofarah SS, *et al.* Composition-driven morphological evolution of $BaTiO_3$ nanowires for efficient piezocatalytic hydrogen production. *Chemosphere* 2023, **338**: 139337.
[59] Li Z, Yang WJ, Xie LB, *et al.* Prominent role of oxygen vacancy for superoxide radical and hydroxyl radical formation to promote

electro-Fenton like reaction by W-doped CeO_2 composites. *Appl Surf Sci* 2021, **549**: 149262.
[60] Liu DM, Zhang JT, Jin CC, *et al.* Insight into oxygen-vacancy regulation on piezocatalytic activity of $(Bi_{1/2}Na_{1/2})TiO_3$ crystallites: Experiments and first-principles calculations. *Nano Energy* 2022, **95**: 106975.
[61] Dong HJ, Zhou YY, Wang LL, *et al.* Oxygen vacancies in piezocatalysis: A critical review. *Chem Eng J* 2024, **487**: 150480.
[62] Zheng Y, Wu XY, Zhang YC, *et al.* Highly efficient harvesting of vibration energy for complex wastewater purification using $Bi_5Ti_3FeO_{15}$ with controlled oxygen vacancies. *Chem Eng J* 2023, **453**: 139919.
[63] Kim MJ, Noh JY, Yun TG, *et al.* Laser-shock-driven *in situ* evolution of atomic defect and piezoelectricity in graphitic carbon nitride for the ionization in mass spectrometry. *ACS Nano* 2022, **16**: 18284–18297.
[64] Hu Y, Rogée L, Wang WZ, *et al.* Extendable piezo/ferroelectricity in nonstoichiometric 2D transition metal dichalcogenides. *Nat Commun* 2023, **14**: 8470.
[65] Wang N, Yang WH, Wang RX, *et al.* Oxygen vacancy-enhanced centrosymmetric breaking of $SrFeO_{3-x}$ for piezoelectric-catalyzed synthesis of H_2O_2. *Small* 2024, **20**: 2307291.
[66] Hu C, Chen F, Wang YG, *et al.* Exceptional cocatalyst-free photo-enhanced piezocatalytic hydrogen evolution of carbon nitride nanosheets from strong in-plane polarization. *Adv Mater* 2021, **33**: 2101751.
[67] Takeda H, Nishida M, Nshida T, *et al.* Growth of bismuth tungstate Bi_2WO_6 mono-domain crystals and chemical etching for measuring their electrical properties. *T MRS JAP* 2007, **32**: 11–14.
[68] Wang ZL, Mao X, Chen P, *et al.* Understanding the roles of oxygen vacancies in hematite-based photoelectrochemical processes. *Angew Chem Int Edit* 2019, **131**: 1042–1046.
[69] Wang SC, He TW, Chen P, *et al. In situ* formation of oxygen vacancies achieving near-complete charge separation in planar $BiVO_4$ photoanodes. *Adv Mater* 2020, **32**: 2001385.
[70] Zhao MJ, Sun ZT, Zhang ZX, *et al.* Suppression of oxygen vacancy defects in sALD–ZnO films annealed in different conditions. *Materials* 2020, **13**: 3910.
[71] Campbell CT, Peden CHF. Oxygen vacancies and catalysis on ceria surfaces. *Science* 2005, **309**: 713–714.
[72] Li XB, Liu Q, Deng F, *et al.* Double-defect-induced polarization enhanced OV–BiOBr/$Cu_{2-x}S$ high-low junction for boosted photoelectrochemical hydrogen evolution. *Appl Catal B-Environ* 2022, **314**: 121502.
[73] Pang B, Liu SC, Tu Y, *et al.* Controllable synthesis and enhanced photoactivity of two-dimensional Bi_2WO_6 ultra-thin nanosheets. *ChemistrySelect* 2021, **6**: 5381–5386.
[74] Li XB, Hu Y, Dong F, *et al.* Non-noble-metallic Ni_2P nanoparticles modified OV–BiOBr with boosting photoelectrochemical hydrogen evolution without sacrificial agent. *Appl Catal B-Environ* 2023, **325**: 122341.
[75] He J, Yi ZR, Chen QQ, *et al.* Harvesting mechanical energy induces piezoelectric polarization of MIL-100(Fe) for cocatalyst-free hydrogen production. *Chem Commun* 2022, **58**: 10723–10726.
[76] Wang CY, Hu C, Chen F, *et al.* Polar layered bismuth-rich oxyhalide piezoelectrics $Bi_4O_5X_2$ (X =Br, I): Efficient piezocatalytic pure water splitting and interlayer anion-dependent activity. *Adv Funct Mater* 2023, **33**: 2301144.
[77] Feng YW, Ling LL, Wang YX, *et al.* Engineering spherical lead zirconate titanate to explore the essence of piezo-catalysis. *Nano Energy* 2017, **40**: 481–486.
[78] Ma H, Yang WJ, Tang HY, *et al.* Enhance the stability of oxygen vacancies in $SrTiO_3$ via metallic Ag modification for efficient and durable photocatalytic NO abatement. *J Hazard Mater* 2023, **452**: 131269.
[79] Ma H, Wang XM, Tan TQ, *et al.* Stabilize the oxygen vacancies in Bi_2SiO_5 for durable photocatalysis via altering local electronic structure with phosphate dopant. *Appl Catal B-Environ* 2022, **319**: 121911.
[80] Chen P, Liu HJ, Sun YJ, *et al.* Bi metal prevents the deactivation of oxygen vacancies in $Bi_2O_2CO_3$ for stable and efficient photocatalytic NO abatement. *Appl Catal B-Environ* 2020, **264**: 118545.
[81] Gao FX, Fang M, Zhang S, *et al.* Symmetry-breaking induced piezocatalysis of Bi_2S_3 nanorods and boosted by alternating magnetic field. *Appl Catal B-Environ* 2022, **316**: 121664.
[82] Bi X, Du GH, Kalam A, *et al.* Tuning oxygen vacancy content in TiO_2 nanoparticles to enhance the photocatalytic performance. *Chem Eng Sci* 2021, **234**: 116440.
[83] Li L, Ma YR, Chen GF, *et al.* Oxygen-vacancy-enhanced piezo-photocatalytic performance of $AgNbO_3$. *Scripta Mater* 2022, **206**: 114234.
[84] Mani AD, Li J, Wang ZQ, *et al.* Coupling of piezocatalysis and photocatalysis for efficient degradation of methylene blue by $Bi_{0.9}Gd_{0.07}La_{0.03}FeO_3$ nanotubes. *J Adv Ceram* 2022, **11**: 1069–1081.
[85] Zhang HM, Wang HL, Tong X, *et al.* Sulfur induced surface reconfiguration of Ni_1Cu_3–S–T/CP anode for high-efficiency ammonia electro-oxidation. *Chem Eng J* 2023, **452**: 139582.
[86] Banoo M, Roy RS, Bhakar M, *et al.* Bi_4TaO_8Cl as a new class of layered perovskite oxyhalide materials for piezopotential driven efficient seawater splitting. *Nano Lett* 2022, **22**: 8867–8874.
[87] Xiao LB, Xu XL, Lu Z, *et al. In-situ* organic–inorganic ferroelectric layer growth for efficient perovskite solar cells with high photovoltage. *Nano Energy* 2023, **107**: 108114.
[88] Kalanur SS, Yoo IH, Seo H. Fundamental investigation of Ti doped WO_3 photoanode and their influence on photoelectrochemical water splitting activity. *Electrochim Acta* 2017, **254**: 348–357.
[89] Yin WJ, Bai LJ, Zhu YZ, *et al.* Embedding metal in the interface of a p–n heterojunction with a stack design for superior Z-scheme photocatalytic hydrogen evolution. *ACS Appl Mater Inter* 2016, **8**: 23133–23142.
[90] Xu XL, Xiao LB, Jia YM, *et al.* Pyro-catalytic hydrogen evolution by $Ba_{0.7}Sr_{0.3}TiO_3$ nanoparticles: Harvesting cold–hot alternation energy near room-temperature. *Energ Environ Sci* 2018, **11**: 2198–2207.
[91] Wang CY, Hu C, Chen F, *et al.* Design strategies and effect comparisons toward efficient piezocatalytic system. *Nano Energy* 2023, **107**: 108093.
[92] Wang YJ, Li X, Chen YK, *et al.* Pulsed-laser-triggered piezoelectric photocatalytic CO_2 reduction over tetragonal $BaTiO_3$ nanocubes. *Adv Mater* 2023, **35**: 2305257.
[93] Wang ZL, Mao X, Chen P, *et al.* Understanding the roles of oxygen vacancies in hematite-based photoelectrochemical processes. *Angew Chem Int Edit* 2019, **58**: 1030–1034.
[94] Fan SQ, Liang YX, Xie JM, *et al.* Exact solutions to the electromechanical quantities inside a statically-bent circular ZnO nanowire by taking into account both the piezoelectric property and the semiconducting performance: Part I—Linearized analysis. *Nano Energy* 2017, **40**: 82–87.
[95] Zhang HY, Wu LL, Feng RH, *et al.* Oxygen vacancies unfold the catalytic potential of NiFe-layered double hydroxides by promoting their electronic transport for oxygen evolution reaction. *ACS Catal* 2023, **13**: 6000–6012.
[96] Wang MY, Zuo YP, Wang JL, *et al.* Remarkably enhanced hydrogen generation of organolead halide perovskites via piezocatalysis and photocatalysis. *Adv Energy Mater* 2019, **9**: 1901801.
[97] Yang FY, Wang PY, Hao JH, *et al.* Ultrasound-assisted piezoelectric photocatalysis: An effective strategy for enhancing hydrogen evolution from water splitting. *Nano Energy* 2023, **118**: 108993.
[98] Jiang YW, Li MZ, Mi Y, *et al.* The influence of piezoelectric effect on the heterogeneous photocatalytic hydrogen production of strontium titanate nanoparticles. *Nano Energy* 2021, **85**: 105949.
[99] Thuy Phuong PT, Zhang Y, Gathercole N, *et al.* Demonstration of enhanced piezo-catalysis for hydrogen generation and water treatment at the ferroelectric curie temperature. *iScience* 2020, **23**: 101095.
[100] Rashwan SS, Dincer I, Mohany A, *et al.* The Sono–Hydro–Gen process (ultrasound induced hydrogen production): Challenges and opportunities. *Int J Hydrogen Energ* 2019, **44**: 14500–14526.